


Cylindrical vector beam-excited frequency-tunable second harmonic generation in a plasmonic octamer

FAJUN XIAO,^{1,*}  WUYUN SHANG,¹ WEIREN ZHU,^{2,3} LEI HAN,¹ MALIN PREMARATNE,³ TING MEI,¹ AND JIANLIN ZHAO^{1,4}

¹MOE Key Laboratory of Material Physics and Chemistry under Extraordinary Conditions, and Shaanxi Key Laboratory of Optical Information Technology, School of Science, Northwestern Polytechnical University, Xi'an 710129, China

²Department of Electronic Engineering, Shanghai Jiao Tong University, Shanghai 200240, China

³Advanced Computing and Simulation Laboratory (A χ L), Department of Electrical and Computer Systems Engineering, Monash University, Clayton, VIC 3800, Australia

⁴e-mail: jlzha@nwpu.edu.cn

*Corresponding author: fxiao@nwpu.edu.cn

Received 24 October 2017; revised 24 December 2017; accepted 28 December 2017; posted 3 January 2018 (Doc. ID 309785); published 9 February 2018

We report a method to tune the second harmonic generation (SHG) frequency of a metallic octamer by employing cylindrical vector beams as the excitation. Our method exploits the ability to spatially match the polarization state of excitations with the fundamental target plasmonic modes, enabling flexible control of the SHG resonant frequency. It is found that SHG of the octamer is enhanced over a broad band (400 nm) by changing the excitation from the linearly polarized Gaussian beam to radially and azimuthally polarized beams. More strikingly, when subjected to an azimuthally polarized beam, the SHG intensity of the octamer becomes 30 times stronger than that for the linearly polarized beam even in the presence of Fano resonance. © 2018 Chinese Laser Press

OCIS codes: (260.5430) Polarization; (190.2620) Harmonic generation and mixing; (250.5403) Plasmonics; (260.6042) Singular optics.

<https://doi.org/10.1364/PRJ.6.000157>

1. INTRODUCTION

Surface plasmons are collective electron oscillations that are bounded to a metal–dielectric interface [1]. These surface waves show a remarkable capability for concentrating the electromagnetic field in the subwavelength scale, and consequently pave a way to enhance the inherently weak light–matter interactions [1]. For example, plasmonic structures have been demonstrated to be ideal platforms for boosting nonlinear optical effects such as second harmonic generation (SHG) [2]. SHG of centrosymmetric noble metals stems from the symmetry breaking at their surfaces [3]. In contrast to conventional nonlinear media, SHG from metal surfaces could get away with phase-matching requirements because of the subwavelength nature of their nonlinear source [3]. Recently, the enhanced SHG has been demonstrated in a variety of metallic structures, such as individual nanoparticles [4,5], nanoantennas [6,7], nanoclusters [8–10], split-ring resonators [11,12] and metamaterials [13,14], promoting applications in frequency converters [2,15,16], super-resolution imaging [17,18], high-performance position [19], and refractive index sensors [20]. Generally, to achieve a high SHG yield,

plasmonic structures are operated at the bright dipolar resonance for the fundamental beam. However, the efficiency of SHG inevitably suffers from the high radiation losses arising from dipolar resonances. Moreover, due to the narrowband response of dipolar resonances, the bright-mode-enhanced SHG exhibits a limited operating frequency, which severely hampers its applications in on-chip nonlinear photonic devices, optical signal generation, and processing. To address the challenge of frequency-tunable SHG, a straightforward way is to mold the geometry of the plasmonic structure to tune the dipolar resonance at the fundamental frequency [21]. Another approach is to use plasmonic structures that support multi-dipolar resonances [22,23]. This method can generate SHG with a considerably broad bandwidth, while resulting in a strong SHG signal through the simultaneous enhancement of the fundamental and double frequency fields. An additional strategy is to change the ambient permittivity to control the SHG frequency by exploiting the fact that the high dielectric constant reduces the restoring force of the plasmon resonance causing a redshift of the resonant frequency [15,24].

In this work, we numerically investigate the frequency-tunable SHG in a metallic octamer. The metallic multimer,

as the inter-particle coupling, possesses very rich plasmonic dark modes with large field enhancement and high Q -factor [25,26]. Therefore, it holds great potential for realizing frequency-tunable SHG by selectively triggering the dark modes. However, owing to the zero dipole moment, plasmonic dark modes are unattainable for conventional linearly polarized beams, hindering their applications in SHG enhancement. Alternatively, we demonstrate the frequency of SHG can be readily tuned by matching the polarization states of excitations with the dark modes of the octamer. Our results facilitate the realization of the integrated nonlinear photonic devices with high frequency tunability.

2. RESULTS AND DISCUSSIONS

Figure 1(a) schematically shows the plasmonic octamer under consideration. This structure is formed by eight silver nanodisks with an equal height of 30 nm placed on a semi-infinite silicon substrate coated with a 100-nm SiO_2 layer. The radii of the central and surrounding nanodisks are 100 nm and 75 nm, respectively. In order to produce a strong coupling between the nanodisks, all gaps between the adjacent disks are set to 15 nm. To study the optical response of the plasmonic octamer, we perform a full-wave simulation by using the finite-difference time-domain (FDTD) commercial software (Lumerical FDTD Solutions). The permittivity of Ag is obtained by empirically fitting the experimental data of Palik with the multi-coefficient model built in the software [27]. The refractive indices of silicon and silicon dioxide are $n_{\text{Si}} = 3.95$ and $n_{\text{SiO}_2} = 1.45$, respectively. The perfectly matched layers as absorbing boundaries are used in our simulation to mimic our designed nanostructure in an infinitely large free space. The simulation scheme shown in Fig. 1(b) considers the plasmonic octamer under excitation of tightly focused x -polarized Gaussian radially and azimuthally polarized vector beams. The electric field of the x -polarized Gaussian beam is written as

$$E_G = E_x \exp[-(x^2 + y^2)/w_0^2], \quad (1)$$

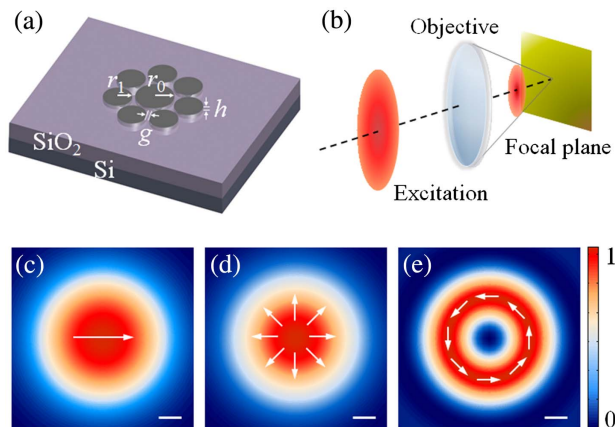


Fig. 1. (a) Schematic view of the Ag octamer on a Si/ SiO_2 substrate. The geometry parameters r_0 , r_1 , g , and h are set as 100, 75, 15, and 30 nm, respectively. (b) Excitation of the octamer with tightly focused beams. Intensities and transverse polarization distributions of (c) x -polarized Gaussian beam, (d) radially and (e) azimuthally polarized beams at the focal plane. The scale bars in (c)–(e) are 200 nm.

where E_x and $w_0 = 500$ nm denote the electric field amplitude and the beam waist, respectively. The electric field of cylindrical vector beams have the form [28]

$$E_v = J_1[\beta(x^2 + y^2)^{1/2}][\cos \phi(x, y)\mathbf{e}_x + \sin \phi(x, y)\mathbf{e}_y]. \quad (2)$$

Here, $J_1(x)$ is the first-order Bessel function of the first kind, β is a constant of 0.4, \mathbf{e}_x and \mathbf{e}_y denote the unit vectors along the x and y directions, and the polarization distribution $\phi(x, y) = \tan^{-1}(y/x) + \phi_0$ is with $\phi_0 = 0, \pi/2$ for radially and azimuthally polarized beams. To keep the same beam diameter at the focal plane, we use the objective with numerical aperture (NA) of 0.9, 0.8, and 0.9 to compress the Gaussian, radially polarized, and azimuthally polarized vector beams, respectively. According to the Richards–Wolf vector diffraction theory [28], we derive the intensities and transverse polarization distributions of the focal fields (on the top surface of the octamer) as shown in Figs. 1(c)–1(e).

In Fig. 2(a), we show the linear scattering spectrum of the octamer under the excitation of the x -polarized Gaussian beam, which is obtained through integrating the electric field intensity over a virtual box enclosing the octamer. An obvious asymmetric lineshape is observed in this scattering spectrum, indicating the occurrence of Fano resonance. The Fano resonance in the plasmonic octamer is produced by the coherent interaction between a dark mode and a bright mode, which can be well interpreted by the plasmonic hybridization theory [29]. The resonance wavelengths of dark and bright modes are determined from the absorption spectrum of the octamer shown in Fig. 2(b), where the broad peak (750–1500 nm) is viewed as the superposition of two Lorentzian peaks. For the dark mode, the dipole moment of peripheral disks is cancelled by

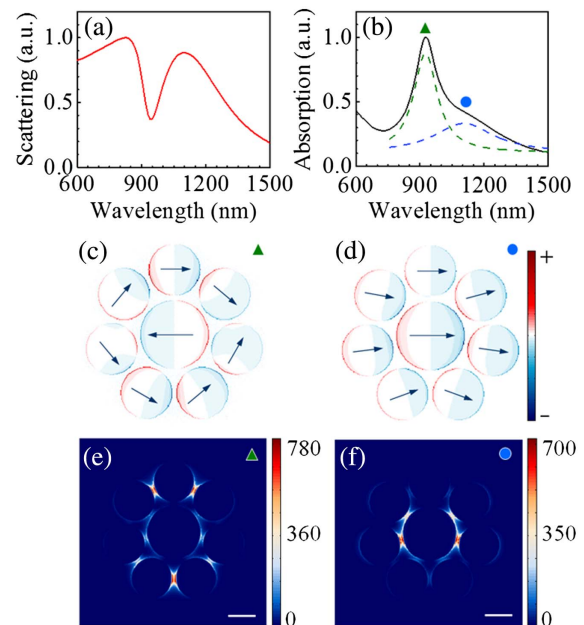


Fig. 2. Normalized (a) scattering and (b) absorption spectra of the octamer under excitation of x -polarized Gaussian beam. Charge distributions for (c) dark and (d) bright modes at the indicated wavelengths in (b). Intensity enhancement maps of (e) dark and (f) bright modes at the top surface of the octamer. The scale bars in (e) and (f) are 100 nm.

that of the central disk, giving rise to a small dipole moment. This can be examined from the charge distribution of the dark mode [Fig. 2(c)], which is obtained by calculating the difference of the normal component of the electric field above and below the Ag surface according to Gauss's law. The bright mode is formed when dipolar plasmons of the central and peripheral disks oscillate in phase [see the charge distribution in Fig. 2(d)]. Because of the near-field coupling of these two modes, scattering lights of the bright and dark modes destructively interfere in the far field, resulting in a minimum in the scattering spectrum represented by a Fano dip around 930 nm. Figures 2(e) and 2(f), respectively, depict the normalized near field distributions of the dark and bright modes, which perfectly match their corresponding dipolar arrangements.

As the strong hybridization leads to a significantly enhanced electric field, plasmonic Fano structures have been widely used to study SHG [9,21,24]. Classically, the SHG sources of plasmonic metals can be considered as a nonlinear polarization $P(2\omega)$ oscillating at the second harmonic frequency. In the electric dipole approximation, this nonlinear polarization can be described as [30]

$$P(r, 2\omega) = \chi^{(2)} : E(r, \omega)E(r, \omega), \quad (3)$$

where $\chi^{(2)}$ and $E(r, \omega)$ correspond to the second-order nonlinear susceptibility and the electric field at fundamental frequency. According to symmetry argument, only the surface susceptibility $\chi_{\perp\perp\perp}^{(2)}$, $\chi_{\perp\parallel\parallel}^{(2)}$, $\chi_{\parallel\perp\perp}^{(2)}$ and $\chi_{\parallel\parallel\perp}^{(2)} = \chi_{\parallel\perp\perp}^{(2)}$ contribute to the SHG field [31], where \perp and \parallel represent the perpendicular and parallel components of the susceptibility tensor, respectively. To calculate the SHG of the octamer, $E(r, \omega)$ is first evaluated at the octamer surface via FDTD simulation. After taking the experimental data of $\chi^{(2)}$ [32], the total SHG field is then obtained through integrating the nonlinear polarization over the structure surface [33].

In Fig. 3(a), we show the SHG spectrum of the octamer under the excitation of the x -polarized Gaussian beam. We further examine the intensity enhancement spectrum at the fundamental frequency as shown in Fig. 3(b), which agrees with the resonance feature of the SHG spectrum. Especially, the nonlinear polarization patterns induced by the dark [Fig. 3(c)] and bright [Fig. 3(d)] modes are almost the same with their corresponding charge distributions at the fundamental frequency [Figs. 2(c) and 2(d)]. Namely, this reveals that the SHG characteristics mainly originate from the resonances at the fundamental frequency. Additionally, as can be seen in Fig. 3(a); the SHG intensity of the dark mode is much stronger than that of the bright mode, owing to the higher local field or lower radiation losses the dark mode has [see in Fig. 3(b)].

We then calculated the linear response of the octamer under illuminations of cylindrical vector beams. Figure 4(a) shows the scattering spectrum of the structure excited by the radially polarized beam. A broad resonance peak is observed and can be decomposed to two Lorentzian peaks located at 540 nm and 680 nm [as the dashed lines shown in Fig. 4(a)]. To further confirm the origins of these two modes, we calculated their charge distributions as shown in Figs. 4(c) and 4(d). Here, both modes have dipolar moments along the radial inward direction as well as the circular nodes (as indicated by dashed lines), resembling the recently found radial breathing mode (RBM) in

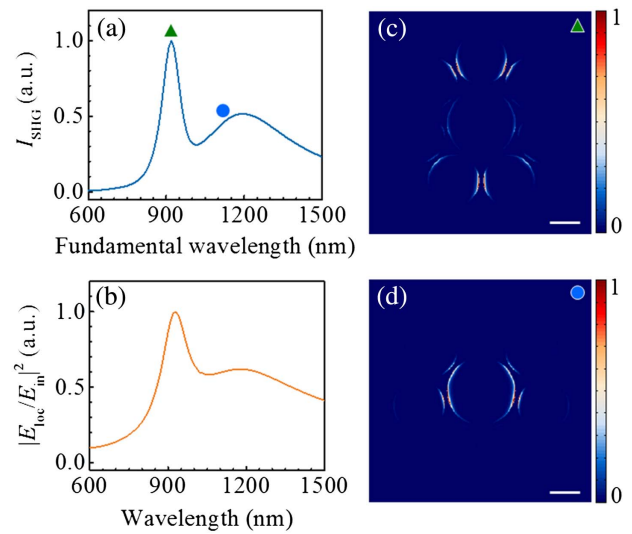


Fig. 3. Normalized (a) SHG and (b) intensity enhancement spectra of the octamer illuminated by the x -polarized Gaussian beam. Normalized nonlinear polarization at the top surface of the octamer excited by the fundamental (c) dark and (d) bright modes. The scale bars in (c) and (d) are 100 nm.

the Ag nanodisk [34]. The radially oscillating characteristics of RBMs are also reflected in the near-field patterns shown in Figs. 4(f) and 4(g), where the electric field is circularly confined at the outer edges of the peripheral disks and edges of the central and peripheral disks along the annulus gap. In addition, these two RBMs, as the charge distributions, show different electron populations, resulting in the disparity in their mode

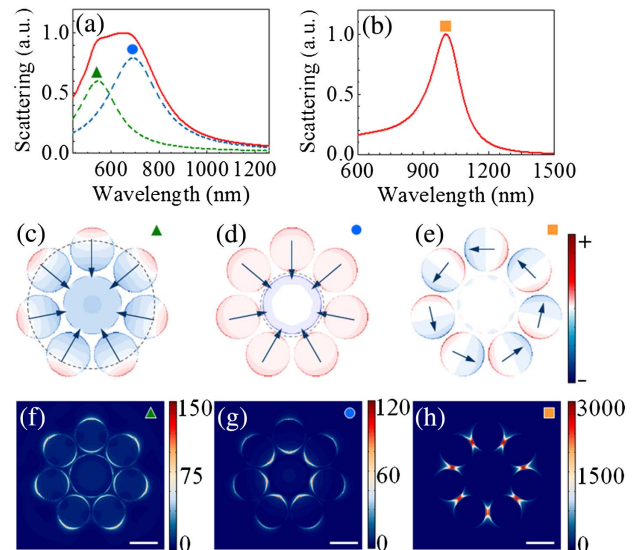


Fig. 4. Normalized scattering spectra of the octamer under excitations of (a) radially and (b) azimuthally polarized vector beams. Charge distributions of (c), (d) radial breathing modes (RBMs) and (e) azimuthally arranged dipolar mode (ADM) at the labeled wavelengths in (a) and (b), respectively. The dashed lines in (c) and (d) represent the node positions of these two modes. Intensity enhancement maps of (f), (g) two RBMs and (h) ADM at the top surface of the octamer. The scale bars in (f)–(h) are 100 nm.

energy. It should be noted that the broad peak in Fig. 4(a) results from the strong coupling between nanodisks. With increasing of the gap size between the central and peripheral nanodisks, this broad peak becomes narrower and eventually evolves to the single peak due to the decreased coupling between nanodisks [35,36].

For the case of the azimuthally polarized beam, a single peak appears at the wavelength of 1000 nm in the scattering spectrum as displayed in Fig. 4(b). We assign this peak to be an azimuthally arranged dipolar mode (ADM), for which the dipole moments of the peripheral disks are arranged in head-to-tail ordering shown in Fig. 4(e). Also, the ADM is revealed by the near-field pattern as depicted in Fig. 4(h), where the electric field is localized between the gaps of peripheral disks. It is noteworthy that both RBMs and ADM possess nearly zero dipole moments, and thus cannot be excited by the conventional linearly polarized beam directly. These dark modes become active due to the spatial matching between the polarization states of excitations and the symmetry of the plasmon modes.

Finally, the SHG from the octamer is investigated when excited by cylindrical vector beams whose beam powers on the octamer surface are set equal to that of the x -polarized Gaussian beam. Figure 5(a) presents the SHG spectrum of the octamer excited by the radially polarized beam. One can clearly see that the SHG resonance is generally consistent with the linear intensity enhancement shown in Fig. 5(c). Also, the nonlinear polarization maps in Figs. 5(e) and 5(f) spatially agree with the charge distributions of their related fundamental RBMs [Figs. 4(c) and 4(d)], which indicates that the resonance of

SHG in Fig. 5(a) mainly arises from field enhancement produced by two RBMs at the fundamental frequency. Moreover, owing to the presence of RBM resonance, the SHG intensity is improved in the fundamental wavelength band of 520–740 nm compared with that excited by the Gaussian beam. Similarly, good agreements are found between the SHG [Fig. 5(b)] and the intensity enhancement spectra [Fig. 5(d)] as well as between the representative nonlinear polarization map [Fig. 5(g)] and its fundamental charge distribution [Fig. 4(e)] for the azimuthally polarized excitation. It is worth noting that under the excitation of the azimuthally polarized beam, the SHG intensity becomes 30 times larger than the case boosted by the dark mode of Fano resonance. At last, the results of Figs. 3 and 5 demonstrate that one can tune the frequency of SHG by selectively excited fundamental plasmonic modes with a suitable polarization state of illumination. Moreover, a broadband (400 nm) enhanced SHG of the octamer is realized when the illumination is changed from a linearly polarized Gaussian beam to radially and azimuthally polarized beams.

3. CONCLUSIONS

In summary, we have theoretically studied the linear and nonlinear responses of a metallic octamer under the excitations with different polarization states, including linearly polarized Gaussian beams, radially polarized beams, and azimuthally polarized beams. In contrast to the case of linearly polarized excitation, two types of highly symmetric dark modes, named RBM and ADM, are selectively excited by the radially and azimuthally polarized beams, respectively. We attribute this plasmonic mode selection to the spatial matching between the polarization state of the illuminations and the dipole moment of the modes. Moreover, a tunable band of field enhancement is achieved as we selectively trigger the plasmonic modes. Strikingly, because of the proportional relation between SHG yield and the square of fundamental field intensity, the SHG frequency can be readily changed when switching the excitation from a linearly polarized Gaussian beam to radially and azimuthally polarized beams. Our results pave the way for the future nonlinear integrated photonic devices with high frequency tunability.

Funding. National Key R&D Program of China (2017YFA0303800); National Natural Science Foundation of China (NSFC) (11634010, 51777168, 61377035, 61675170, 61675171, 61701303); Australian Research Council (ARC) (DP140100883); Natural Science Basic Research Plan in Shaanxi Province, China (2017JM6022); Fundamental Research Funds for the Central Universities, China (3102017zy017); Natural Science Foundation of Shanghai, China (17ZR1414300); Shanghai Pujiang Program, China (17PJ1404100).

REFERENCES

1. M. Premaratne and M. Stockman, "Theory and technology of SPASERS," *Adv. Opt. Photon.* **9**, 79–128 (2017).
2. J. Lee, M. Tymchenko, C. Argyropoulos, P. Y. Chen, F. Lu, F. Demmerle, G. Boehm, M. Amann, A. Alu, and M. A. Belkin, "Giant nonlinear response from plasmonic metasurfaces coupled to intersubband transitions," *Nature* **511**, 65–69 (2014).

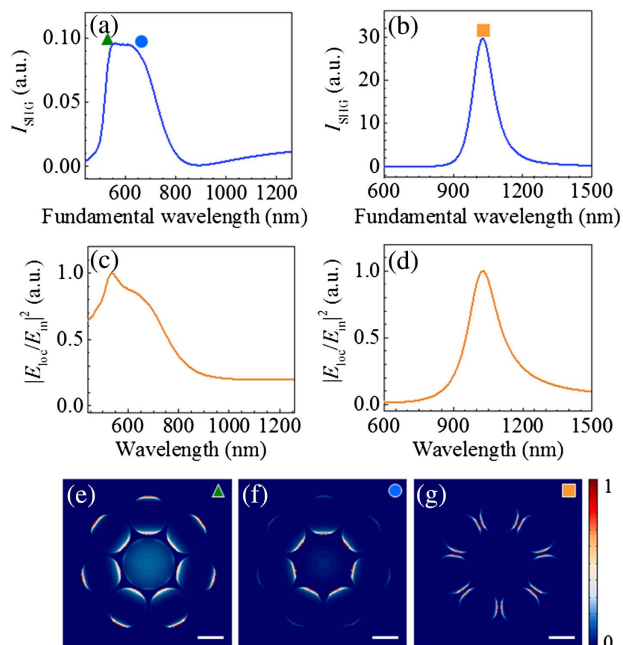


Fig. 5. (a), (b) SHG spectra of the octamer normalized by the maximum value of SHG intensity produced by the x -polarized Gaussian beam. (c), (d) Intensity enhancement spectra of the octamer. Here, (a), (c) and (b), (d) are under the excitations of the radially and azimuthally polarized beams, respectively. Normalized nonlinear polarization at the top surface of the octamer excited by the fundamental (e), (f) RBMs and (g) ADM. The scale bars in (e)–(g) are 100 nm.

3. M. Kauranen and A. V. Zayats, "Nonlinear plasmonics," *Nat. Photonics* **6**, 737–748 (2012).
4. J. Butet, J. Duboisset, G. Bachelier, I. Russierantoine, E. Benichou, C. Jonin, and P. O. Brevet, "Optical second harmonic generation of single metallic nanoparticles embedded in a homogeneous medium," *Nano Lett.* **10**, 1717–1721 (2010).
5. C. Ciraci, E. Poutrina, M. Scalora, and D. R. Smith, "Second-harmonic generation in metallic nanoparticles: clarification of the role of the surface," *Phys. Rev. B* **86**, 115451 (2012).
6. T. Onuta, M. Waegeler, C. Dufort, W. L. Schaich, and B. Dragnea, "Optical field enhancement at cusps between adjacent nanoapertures," *Nano Lett.* **7**, 557–564 (2007).
7. T. Hanke, G. Krauss, D. Trautlein, B. Wild, R. Bratschitsch, and A. Leitenstorfer, "Efficient nonlinear light emission of single gold optical antennas driven by few-cycle near-infrared pulses," *Phys. Rev. Lett.* **103**, 257404 (2009).
8. A. Capretti, G. F. Walsh, S. Minissale, J. Trevino, C. Forestiere, G. Miano, and L. Dal Negro, "Multipolar second harmonic generation from planar arrays of Au nanoparticles," *Opt. Express* **20**, 15797–15806 (2012).
9. K. Thyagarajan, J. Butet, and O. J. F. Martin, "Augmenting second harmonic generation using Fano resonances in plasmonic systems," *Nano Lett.* **13**, 1847–1851 (2013).
10. B. K. Canfield, H. Husu, J. Laukkanen, B. Bai, M. Kuittinen, J. Turunen, and M. Kauranen, "Local field asymmetry drives second-harmonic generation in noncentrosymmetric nanodimers," *Nano Lett.* **7**, 1251–1255 (2007).
11. M. W. Klein, C. Enkrich, M. Wegener, and S. Linden, "Second-harmonic generation from magnetic metamaterials," *Science* **313**, 502–504 (2006).
12. S. Linden, F. B. P. Niesler, J. Forstner, Y. Grynko, T. Meier, and M. Wegener, "Collective effects in second-harmonic generation from split-ring-resonator arrays," *Phys. Rev. Lett.* **109**, 015502 (2012).
13. H. Husu, R. Siikanen, J. Makitalo, J. Lehtolahti, J. Laukkanen, M. Kuittinen, and M. Kauranen, "Metamaterials with tailored nonlinear optical response," *Nano Lett.* **12**, 673–677 (2012).
14. B. Wang, R. Wang, R. J. Liu, X. Lu, J. Zhao, and Z. Li, "Origin of shape resonance in second-harmonic generation from metallic nanohole arrays," *Sci. Rep.* **3**, 2358 (2013).
15. S. Lan, S. P. Rodrigues, Y. Cui, L. Kang, and W. Cai, "Electrically tunable harmonic generation of light from plasmonic structures in electrolytes," *Nano Lett.* **16**, 5074–5079 (2016).
16. K. O. Brien, H. Suchowski, J. Rho, A. Salandrino, B. Kante, X. Yin, and X. Zhang, "Predicting nonlinear properties of metamaterials from the linear response," *Nat. Mater.* **14**, 379–383 (2015).
17. V. K. Valev, A. Silhanek, N. Smisdom, B. De Clercq, W. Gillijns, O. A. Aktsipetrov, M. Ameloot, V. Moshchalkov, and T. Verbiest, "Linearly polarized second harmonic generation microscopy reveals chirality," *Opt. Express* **18**, 8286–8293 (2010).
18. G. Bautista, M. J. Huttunen, J. M. Kontio, J. Simonen, and M. Kauranen, "Third- and second-harmonic generation microscopy of individual metal nanocones using cylindrical vector beams," *Opt. Express* **21**, 21918–21923 (2013).
19. J. Butet and O. J. F. Martin, "Nonlinear plasmonic nanorulers," *ACS Nano* **8**, 4931–4939 (2014).
20. J. Butet, I. Russierantoine, C. Jonin, N. Lascoux, E. Benichou, and P. Brevet, "Sensing with multipolar second harmonic generation from spherical metallic nanoparticles," *Nano Lett.* **12**, 1697–1701 (2012).
21. G. F. Walsh and L. Dal Negro, "Enhanced second harmonic generation by photonic-plasmonic Fano-type coupling in nanoplasmonic arrays," *Nano Lett.* **13**, 3111–3117 (2013).
22. H. Aouani, M. Navarrocia, M. Rahmani, T. P. H. Sidiropoulos, M. H. Hong, R. F. Oulton, and S. A. Maier, "Multiresonant broadband optical antennas as efficient tunable nanosources of second harmonic light," *Nano Lett.* **12**, 4997–5002 (2012).
23. S. Liu, E. S. P. Leong, G. Li, Y. Hou, J. Deng, J. Teng, H. C. Ong, and D. Y. Lei, "Polarization-independent multiple Fano resonances in plasmonic nonamers for multimode-matching enhanced multiband second-harmonic generation," *ACS Nano* **10**, 1442–1453 (2016).
24. F. Xiao, W. Zhu, W. Shang, T. Mei, M. Premaratne, and J. Zhao, "Electrical control of second harmonic generation in a graphene-based plasmonic Fano structure," *Opt. Express* **23**, 3236–3244 (2015).
25. J. B. Lassiter, H. Sobhani, M. W. Knight, W. S. Mielczarek, P. Nordlander, and N. J. Halas, "Designing and deconstructing the Fano lineshape in plasmonic nanoclusters," *Nano Lett.* **12**, 1058–1062 (2012).
26. A. Yanai, M. Grajower, G. M. Lerman, M. Hentschel, H. Giessen, and U. Levy, "Near- and far-field properties of plasmonic oligomers under radially and azimuthally polarized light excitation," *ACS Nano* **8**, 4969–4974 (2014).
27. E. D. Palik, *Handbook of Optical Constants of Solids* (Academic, 1985).
28. Q. Zhan, "Cylindrical vector beams: from mathematical concepts to applications," *Adv. Opt. Photon.* **1**, 1–57 (2009).
29. E. Prodan, C. Radloff, N. J. Halas, and P. Nordlander, "A hybridization model for the plasmon response of complex nanostructures," *Science* **302**, 419–422 (2003).
30. Y. R. Shen, *The Principles of Nonlinear Optics* (Wiley, 1973).
31. J. I. Dadap, J. Shan, K. B. Eisenthal, and T. F. Heinz, "Second-harmonic Rayleigh scattering from a sphere of centrosymmetric material," *Phys. Rev. Lett.* **83**, 4045–4048 (1999).
32. D. Krause, C. W. Teplin, and C. T. Rogers, "Optical surface second harmonic measurements of isotropic thin-film metals: gold, silver, copper, aluminum, and tantalum," *J. Appl. Phys.* **96**, 3626–3634 (2004).
33. S. Tang, D. Cho, H. Xu, W. Wu, Y. R. Shen, and L. Zhou, "Nonlinear responses in optical metamaterials: theory and experiment," *Opt. Express* **19**, 18283–18293 (2011).
34. F. Schmidt, H. Ditlbacher, U. Hohenester, A. Hohenau, F. Hofer, and J. R. Krenn, "Dark plasmonic breathing modes in silver nanodisks," *Nano Lett.* **12**, 5780–5783 (2012).
35. M. Hentschel, D. Dregely, R. Vogelgesang, H. Giessen, and N. Liu, "Plasmonic oligomers: the role of individual particles in collective behavior," *ACS Nano* **5**, 2042–2050 (2011).
36. J. Ye, F. Wen, J. Lassiter, H. Sobhani, P. Van Dorpe, P. Nordlander, and N. Halas, "Plasmonic nanoclusters: near field properties of the Fano resonance interrogated with SERS," *Nano Lett.* **12**, 1660–1667 (2012).